This is a repository copy of *Continuously variable diffraction gratings using electroconvection in liquid crystals for beam steering applications*.

White Rose Research Online URL for this paper:
http://eprints.whiterose.ac.uk/153452/

Version: Accepted Version

Continuously variable diffraction gratings using electroconvection in liquid crystals for beam steering applications

R. Morris, J.C. Jones and M. Nagaraj*

School of Physics and Astronomy, University of Leeds, Leeds, West Yorkshire, LS2 9JT, UK.

There is a great technological need for the development of devices capable of producing wide-angle and efficient, transmissive optical beam steering. In this article, variable pitch phase diffraction gratings using electroconvection in liquid crystals are considered for applications in electrically controllable beam-steerers. The devices contain thin layers of nematic liquid crystal mixtures of negative dielectric anisotropy, which are doped with different concentrations of an ionic species to determine the effect of conductivity on the beam-steering characteristics. The devices are seen to act as continuously variable diffraction gratings, where the pitch increases with the frequency of the applied electric field. The second order diffraction peak are found to be most efficient, with absolute efficiency ranging from 5% to 15%, and continuous steering from 4° to 8° within 20 µm spaced devices is demonstrated. Devices with thinner layers of liquid crystal were also examined; these demonstrated wider angle steering but had substantial losses of efficiency, due to a lowering of optical contrast. Suggestions for possible methodologies for optimizing such devices are discussed.

I. Introduction

The study of pattern formation in systems at dynamic equilibrium is of fundamental importance across a range of scientific disciplines, including thermodynamics[1], cosmology[2], and Newtonian mechanics[3]. Such effects are typically caused by competition of action and dissipation[4]. Liquid Crystals (LCs) are useful systems to investigate dynamic equilibrium and pattern formation, as they offer large response functions and accessible time and length scales for patterns to form[5]. Study of such instabilities is therefore useful, for both fundamental science, and potentially the design of practical optical devices.

Since 1963, when Williams[6] demonstrated the electrically induced scattering of light using LCs, and the subsequent design of the first Liquid Crystal Display (LCD) in 1968 by Heilmeier[7], liquid crystals have shown suitability as a display medium. Almost all LCDs operate by modulating polarised light using the electro-optic effect of an LC material, famously used in the twisted nematic LCD[8]. Recent decades have led to an increased interest in the use of LCs as switchable optical materials in non-display devices such as, smart windows, adaptive lenses[9–12] and spatial light modulators(SLMs) [13–16]. The interest in LC SLMs is driven in part by the limitations of other existing SLM technologies, which commonly utilize Micro Electrical Mechanical System (MEMS) mirrors. These MEMS mirrors are capable of short switching times (>60 kHz) and relatively small pixel sizes (<20 μm) [17]; however, have the drawback of operating in reflection mode only restricting certain applications[18]. Liquid crystals are attractive because they exhibit good switching speeds, are well suited to compact devices and can be utilized in transmissive devices[14,18–20].

LC SLMs can be designed using a wide variety of modes[13], but usually, modulate incident polarised light and reorient the LC optic axis using an electric field[21]. Controlling this applied field in a spatially dependent manner defines the optical phase of the emergent light spatially, allowing optical elements including lenses[9,22,23], diffraction gratings[24,25] and beam steering devices [19] to be fabricated. For high-quality LC SLMs, liquid crystal on silicon (LCoS) technology is frequently used[14,25], since this allows pixel sizes below 5 µm[26,27] to be addressed. Similarly to MEMS systems, LCoS has the disadvantage that it can operate in reflection mode only due to the silicon backplane required for driving circuitry. Transmissive devices are larger as they use polysilicon on glass for the Thin Film Transistor (TFT) drivers, resulting in a minimum pixel size of around 10 µm; this limits transmissive LC SLM use as maximum optical interaction occurs when the pixel size is comparable with the wavelength of light[28,29], restricting attainable angles. Due to this, reducing minimum transmissive pixel size is a current technological challenge to be achieved. Other LC devices have achieved efficient, wide-angle steering. However, these are fashioned using surface treatment or geometric means, meaning steering angle cannot be continuously varied[30–32]. Overall there is a technological need for the development of devices capable of wide-angle and efficient, transmissive optical beam steering.

In this work, a detailed investigation of liquid crystals forced into a state of electro-hydro-dynamic-instability (EHDI) for beam steering applications, is provided. In a EHDI state, the dielectric and conductive elements of the material compete, causing a breaking of symmetry, as pattern formation occurs. The paper is structured as follows. Firstly, an analysis of EHDI formation in nematic LCs, as an approach to produce short-pitch diffraction gratings is presented. Secondly, the effect of doping the LC material using an ionic salt is described, as a method to improve the uniformity and quality of textures; hence the relationship between device function and the concentration of the dopant and spacings is found. In the last section, the diffraction an assessment of the grating's ability to continuously and efficiently steer beams is presented.

II. Theory

A. The standard model of electroconvection

To design and optimize the SLM device, an understanding of EHDI formation and resultant optical effects is first required. EHDI (or electroconvection, EC), is most simply described for a nematic LC with a negative dielectric anisotropy $(\varepsilon_{\parallel}-\varepsilon_{\perp}= \Delta\varepsilon<0)$ and positive conductivity anisotropy $(\sigma_{\parallel}-\sigma_{\perp}= \Delta\sigma>0)$, in a planar aligned device with electric field applied normal to enclosing substrates (z) (figure 1(a)). Within this system, consider the unit vector, $\mathbf{n}$, which is the average orientation of molecular long-axis at a point in space, commonly called the director (the symbols $\parallel$ and $\perp$ indicate the material properties measured parallel and perpendicular to $\mathbf{n}$ respectively)[5]. When a critical voltage (V_C) is applied to a device such as that shown in figure 1a, a positive feedback loop is instigated. Here, a localized fluctuation in the director will lead to a positive feedback loop, where convective rolls will form analogously to thermally driven Rayleigh-Bernard convection effect[4,33]. As the charges of either type are separated by being grouped into these flows of ions, an in-plane electric field is created (parallel to x in figure 1b, from red to blue arrows, see in rotating regimes). As the material has a negative $\Delta\varepsilon$, it will reorient the director towards the z-axis, similar to the famous Fréedericksz transition[21,34,35]. This is known as the Carr-Helfrich mechanism[36,37] and causes the formation of a textured EHDI state of period λ_C (figure 1(b)). It is common practice to convert λ_C into a wavenumber, q_C, where,

$$q_C = \frac{2\pi}{\lambda_C}. \tag{1}$$

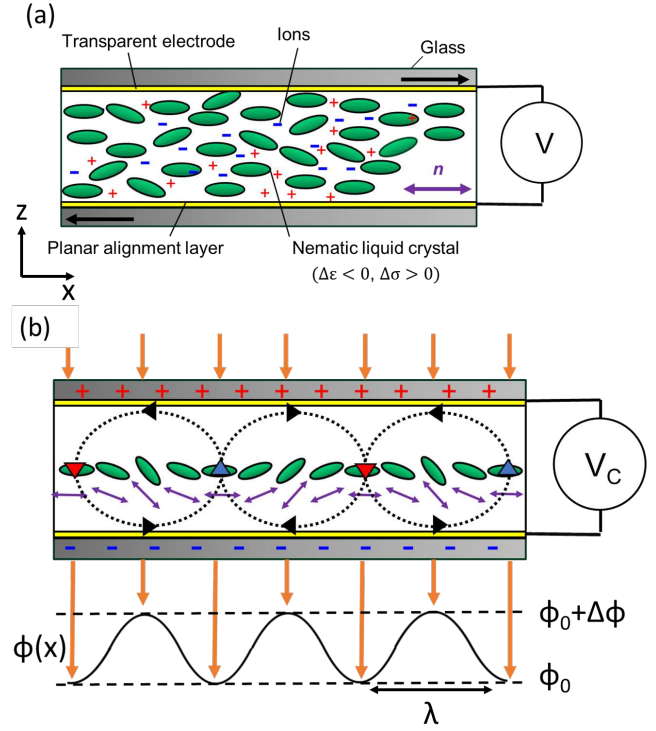FIG. 1 (a) Schematic of a device with no voltage applied. It consists of two glass substrates held in the xy plane. These are coated with a transparent conductor (Indium Tin Oxide) and planar alignment polymer, which is rubbed in the direction shown by black arrows giving alignment of $\mathbf{n}$ approximately parallel to x. Also shown is a cartoon of constituent molecules (green) with the associated director, $\mathbf{n}$, which will be uniform throughout. (b) Snapshot of the device at the critical voltage (V_C) applied. Here ionic flow (shown by arrows on circles) leads to a periodic charge separation in the x-direction, where blue and red arrows represent concentrated regions of negative and positive charge respectively. This reorients the director (double-headed purple arrows) due to the in-plane field created. Orange lines parallel to the z-direction, are rays of light which gain a phase $\phi(x)$ as they pass through the material. The emergent phase varies between ϕ_0 and $\phi_0+\Delta\phi$, where ϕ_0 is the phase acquired at all points in part (a). This dependence of ϕ with x is due to the coupling of the director to material refractive index, allowing the device to act as a phase diffraction grating with period λ.

When viewed using Polarising Optical Microscopy (POM), the device shown in figure 1a will exhibit different liquid crystal textures depending on the frequency and magnitude of the applied voltage(V). Figure 2 shows the expected characteristic pattern morphology of a device such as that shown in figure 1a, with optical microscopy images. Samples typically have two regimes in the voltage - frequency space, corresponding to low frequency 'conductive' and high frequency 'dielectric'[38-40] regimes. This work focusses on the conduction regime.
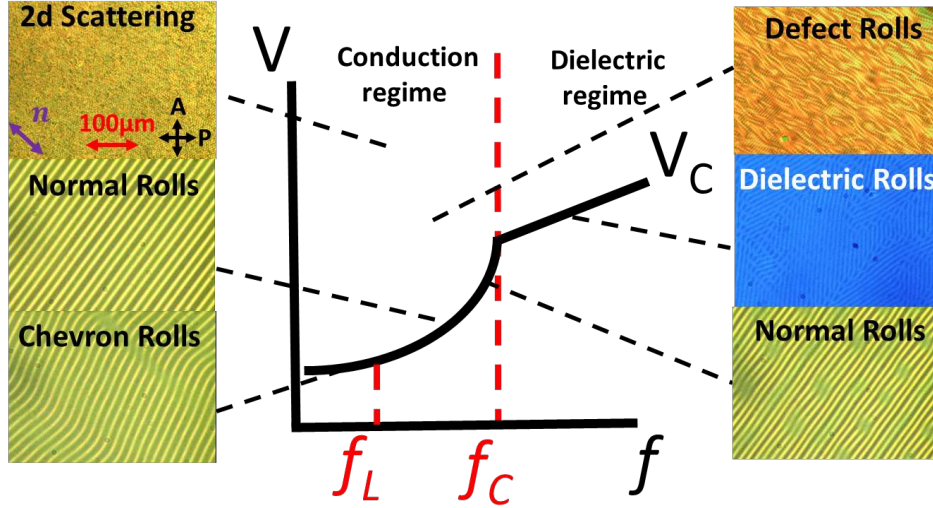
FIG. 2 *Shows the typical behavior of critical voltage (V_C) as frequency (f) is varied in the device, such as that in figure 1a. Also shown are examples of the resulting POM textures. The scale bar, rubbing direction and polarizer orientations are the same for all pictures. The two regimes, low frequency 'conduction' and the high frequency 'dielectric' are shown, the boundary between the regimes marked with f_C. At lower frequencies, there is another critical frequency known as the Lifshitz point (f_L), where 'chevron rolls' will appear as opposed to 'Normal rolls'* [35].

In the formation of an EHDI, the material's electronic and viscoelastic properties will influence V_C and q_C as the frequency is varied. Using the standard model of electroconvection, the following relationship can be ascertained[35,36,38,39]:

$$V_C^2 = \frac{\pi^2 K^{eff}}{\varepsilon_0 \Delta \varepsilon^{eff} + I_h \frac{\left(\frac{\alpha_3}{q_C^2} - \alpha_2\right)\tau_q \Delta \sigma^{eff}}{\eta^{eff}}}, \quad (2)$$

where q_C is the wave number of the resulting rolls; K^{eff}, $\varepsilon_0 \Delta \varepsilon^{eff}$, $\Delta \sigma^{eff}$ and η^{eff} are the effective, one constant elasticity, dielectric anisotropy, conductive anisotropy and viscosity as functions of f, respectively, α_3 and α_2 are the material Leslie coefficients, and I_h is a constant. τ_q is a charge relaxation time, related to the permittivity and conductivity through:

$$\tau_q = \frac{\varepsilon_0 \varepsilon_\perp}{\sigma_\perp}, \quad (3)$$

where $\varepsilon_\perp$ and $\sigma_\perp$ are the permittivity and conductivity perpendicular to the director, respectively (z-direction in figure 1a). Equation 2 identifies the key role of $\Delta\sigma^{eff}$ in the formation of EHDI states, where typically small quantities of ionic impurities within the material provide free charge carriers allowing the Carr-Helfrich mechanism to occur[36,37,39]. When studying electroconvection, it is common practice to dope the materials with additional ionic species to enhance $\Delta\sigma$ controllably, increasing the ease at which EDHI states are observed [39,41,42]. This has been shown to have other advantages of increasing the uniformity of the resulting optical textures[42] and the value f_c (see figure 2) [39], meaning the conduction regime can be observed more clearly and over a wider range of frequencies. Eqn. 2 implies that V_C and q_C will mutually increase with the frequency of applied voltage[38,39,42]. Rearranging Eqn 2, it can be stated that if the following inequality is satisfied:

$$\frac{1}{q_c} \gg \sqrt{\frac{\varepsilon_0 \Delta \varepsilon^{eff} \eta^{eff}}{I_h \alpha_3 \tau_q \Delta \sigma^{eff}} - \frac{\alpha_2}{\alpha_3}}, \quad (4)$$

then

$$V_C(f) \sim q_C(f). \quad (5)$$

This indicates that mutual modulation of voltage and frequency allows continually variable diffraction effects to be created.

B. Nematic LCs in the EHDI state as diffraction gratings

Much work has been carried out previously to analyze the diffraction of light passed through a nematic LC layer in an EHDI state[42-45]. In such work, it was usually assumed that light passing through a device acquires an optical phase (ϕ)[42]:

$$\phi(r) = k_\lambda \int_0^d n_{eff}(r) dz, \quad (6)$$

where k is the wave number of transmitted light and $n_{eff}(r)$ is the effective refractive index at position r in space, calculated using:

$$n_{eff}(\mathbf{r}) = \frac{n_o n_e}{\sqrt{n_o^2 cos^2\psi(\mathbf{r}) + n_e^2 sin^2\psi(\mathbf{r})}} \ , \qquad (7)$$

and n_o and n_e are the LC ordinary and extraordinary refractive indices, and ψ is the deflection angle of the director from the xy plane. For the normal roll pattern seen in figures 1 and 2, it is common to approximate ψ to be[42,44]:

$$\psi(x,z) = \psi_{max} sin\left(\frac{2\pi x}{\lambda_C}\right) sin\left(\frac{\pi z}{d}\right), \qquad (8)$$

where x and z are the cartesian coordinates of the device and ψ_{max} is the maximum director reorientation from x-axis towards the z-axis. As shown in figure 1b, this causes a variance in $\phi(x)$ resulting in diffraction. It has been shown that to a first approximation, the diffraction angles can be described using Bragg's equation[35,46];

$$sin\theta_m \approx \frac{mq_c}{k_\lambda}, \qquad (9)$$

where m and θ_m are a diffraction order's number and angle, respectively. Combining equations (6) to (8), John et al.[42], calculated the phase of emergent light as a function of x:

$$\phi(x) = \frac{k_\lambda n_e d(n_e^2 - n_o^2) sin\left(\frac{4\pi x}{\lambda_C}\right)}{8n_o^2} \psi_{max}^2. \qquad (10)$$

Previously, it has been found in several published works[42,43], that the $m=2$ order is most efficient. Assuming the liquid crystal layer is sufficiently thin, John et al. calculate the relative efficiency (η) of the second order to be[42]:

$$\eta_{m=2} = \frac{I_2}{I_0} = \frac{1}{4}\left[\frac{k_\lambda n_e d(n_e^2 - n_o^2)}{8n_o^2}\right]^2 \psi_{max}^4 \ , \qquad (11)$$

where $\eta_{m=2}$ is the relative magnitude of the 2nd order diffraction peaks. From Eqn 11, ψ_{max} can be identified as the dominant parameter to optimize to create an efficient device. Intuitively, this indicates that placing a large torque on the director is desirable.

III. Method

A. Overview of work

This work presents the use of a negative $\Delta\varepsilon$ liquid crystal mixture doped with ionic species for enhanced electroconvection. Firstly, changes in permittivity and conductivity due to the addition of ionic species are characterized using dielectric spectroscopy. Secondly, measurements are presented of q_c and V_C as the frequency is varied using polarising optical microscopy. Finally, results from diffraction experiments, characterizing the ability of devices to steer optical beams continuously and efficiently are given. The work is concluded with an overview of device

function, with potential methodologies to optimize technology for commercial devices.

B. Device fabrication and characterization

The liquid crystal material chosen for this work was MLC 2081 (Merck Chemicals, UK). This was chosen due to, properties of negative $\Delta\varepsilon$, wide nematic range (-40°C to 108°C), moderate birefringence (n_e=1.7037 and n_o=1.5031 at measured T=20°C with 589.3nm laser) and low intrinsic conductivity. The ion used was Tetra-Butyl-Ammonium-Tetra-Phenyl-Borate (TBATPB, Sigma Aldrich) and is shown in figure 3. TBATPB was chosen as it has previously proved to exhibit good solubility and enhance conductivity in liquid crystalline host materials[41,47].

FIG.3 The ionic additive used (Tetra-Butyl-Ammonium-Tetra-Phenyl-Borate, TBATPB).

Five mixtures of mass fractions (Φ) between 0.3wt.% and 2.3 wt. % TBATPB in MLC 2081 were created. Each mixture and the pure host LC material was then placed within a uniformly spaced 19.5 ± 0.6μm device (supplied by The Military University of Technology, Warsaw, Poland). The devices consisted of two glass plates coated with a conductive ITO layer for application of electric field, and a thin coating of antiparallel rubbed polyimide (SE130) for planar homogeneous alignment purposes. Two similar thinner devices of 10.0±0.2μm and 4.9±0.2μm spacing were filled with a 0.6% TBATPB MLC 2081 mixture, in order to investigate the effect of device spacing. Homeotropic cells were also studied, both with the negative $\Delta\varepsilon$ mixture MLC 2081, and the positive $\Delta\varepsilon$ liquid crystal E7. In either case, the homeotropic alignment was found to degrade rapidly in all samples that included the mobile ions TBATPB, when a low frequency (<500Hz) electric field was applied. This indicates that the degradation was neither due to the Fréedericksz transition or hydrodynamic effects, but due to ion adsorption onto the surface, although the effect is not understood. Hence, dielectric characterization was only accurate for the pure MLC 2081 in the homeotropic geometry. Similar degradation was not observed in the planar-aligned cells over the timescales of the experiments.

The devices were characterized before and after filling using dielectric spectroscopy at temperatures between 25°C to 145 °C, using an LCR meter (Agilent E4980A), with coupled hotstage (Linkham TMS93). An oscillator level of 0.05V was used, and frequency scans completed between 20Hz and 2MHz, finding values of capacitance (C), conductance (G) and loss tangent ($tan\delta$). In these frequency scans, flat plateau regions in C an G were identified far from any relaxation processes through monitoring $tan\delta$. These were taken as the device values, and converted into the

material parameters: permittivity ($\varepsilon'_\perp$) and conductivity ($\sigma_\perp$), both perpendicular to **n**, using standard equations for two parallel plates:

$$\varepsilon'_\perp = \frac{C}{C_0} \quad (12)$$

and

$$\sigma_\perp = \frac{Gd}{A}, \quad (13)$$

where C_0 is the capacitance before filling, d is the device spacing, and A is the electrode area.

C. Device function analysis

Polarising optical microscopy was used to measure V_C and q_C as functions of frequency for all planar samples at 26°C. In each case, a sinusoidal waveform of set frequency (f) was applied while slowly increasing the voltage to the critical value V_C, where the characteristic texture became evident. At this point, the period of the rolls (λ_C) was measured with a stage micrometer to obtain q_C (see equation 1). Between each measurement, the applied voltage was removed entirely and slowly increased from a value far lower than the previous level to prevent hysteresis.

Diffraction experiments were also carried out at ambient laboratory temperatures(~17 °C). The device was illuminated at normal incidence by a HeNe laser (628 nm), and, at a set frequency, the voltage was slowly increased until a diffraction pattern became evident. Each mth order was characterized in terms of deflection angle (θ_m) and absolute diffraction efficiency (ξ_m)[29]. For measurements of ξ_m, a beam profiler (Thorlabs, BC106N-VIS) was used to obtain a 2-dimensional spatial distribution of intensity $I(x,y)$. $I(x,y)$ was then converted into cylindrical coordinates (R,θ) about the center of the m=0 order. $I_\theta(R)$ was first viewed to identify peak locations, where:

$$I_\theta(R) = \int_0^{2\pi} (I(R,\theta) - I_0)d\theta, \quad (14)$$

R is the distance from the center of the diffraction pattern and I_0 is the background noise intensity. The intensity of peaks (I_m) were obtained for the mth orders using:

$$I_{m=0} = \int_0^{R_{f,m}} I_\theta(R)dR \ , \quad (15)$$

and

$$I_{m\neq 0} = \frac{1}{2}\int_{R_{i,m}}^{R_{f,m}} I_\theta(R)dR. \quad (16)$$

Here, $R_{i,m}$ and $R_{f,m}$ are the locations of minima in intensity before and after the mth peak respectively. The factor ½ in equation (16) is due to averaging of ±m peaks when cylindrical coordinates are used. Absolute efficiencies were found from the peak size relative to the rest of the field of view, using,

$$\xi_m = \frac{I_m}{\int_0^{Rmax} I_\theta(R)dR}, \quad (17)$$

where R_{max} is the maximum value for R. This assumes negligible losses both through reflection on substrates and through scattering effects in the device.

IV. Results and Discussion

A. Enhancement of device conductivity

It was found that TBATPB had the desired effect of enhancing material conductivity, with all doped samples having greater conductivity than the pure MLC 2081. Within doped samples, when frequency-dependent scans were performed to attain $C(f)$ and $G(f)$, there was evidence of a formation of a Helmholtz double layer (characterized by low-frequency decrease in G[48,49]) and electrode polarisation (characterized by a low-frequency increase in C[50]). The frequencies above which these effects had relaxed were dependent on temperature and salt concentration, as the characteristic plateaued region moved to higher frequencies with both higher salt concentration and temperature. This was attributed to the increased availability of free charge carriers due to higher thermal energy, and a lowering of material viscosity.
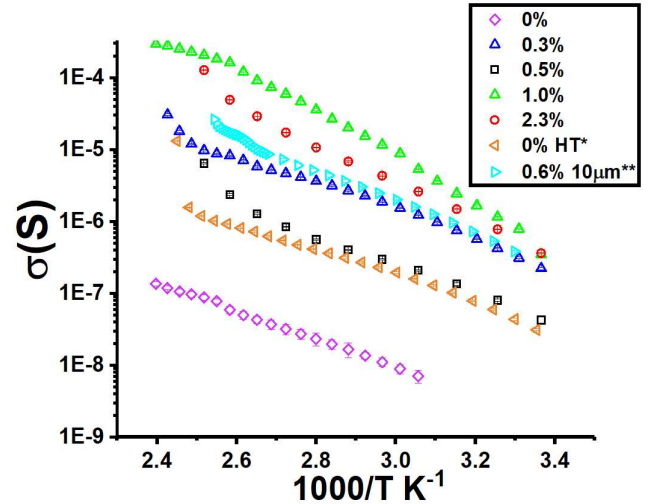

FIG. 4 *Shows plot of measured conductivity of MLC 2081 doped with TBATPB as a function of inverse temperature. These data sets are taken from frequency dependent scans, where plateaued conductance values were taken and converted to conductivity with equation (13). First 5 devices marked; 0%, 0.3%, 0.5%, 1.0% and 2.3% are 20μm planar aligned cells with indicated concentration TBATPB. "0%HT*" is the pure MLC 2081 in a 20μm cell with homeotropic alignment and "0.6% 10μm**" is 0.6% TBATPB MLC 2081 in a 10μm spaced device. This data was fitted with equation 18 to give values σ_0.*

Figure 4 shows a plot of the conductivity plateaus from the frequency scans as a function of inverse temperature. Here, the plots are approximately linear at temperatures sufficiently below the nematic to isotropic transition

temperature (T_{NI}). This data was fit with the Arrhenius expression,

$$\sigma = \sigma_0 e^{-\frac{E_A(T)}{k_B T}}, \qquad (18)$$

where σ_0 is the value of σ as $1/T$ tends to zero, E_A is a activation energy, and k_B is Boltzmann's constant.

Table I shows results of dielectric characterization of the planar 5 μm, 10 μm and 20 μm devices and the homeotropic 20μm device. Here, the samples are ranked in terms of values σ_0 instead of mass faction, Φ. This is due to the values σ_0, being considered as a more reliable measure of dissolved ion content. In measurements of permittivity, the addition of TBATPB led to no significant change in permittivity values($\varepsilon' = 6.3\pm0.3$ at 26°C in all 20 μm planar devices).

B. Polarising optical microscopy

Figures 5a and b, show results for $V_C(f)$ and $q_C(f)$ in samples #1-5, taken at T=26°C. In all doped samples, both $V_C(f)$ and $q_C(f)$ have approximate fourth power dependencies on the frequency of the applied field, and are fitted with the simple empirical fittings that we found to be sufficient to model the data and make comparisons:

$$V_C(f) = V_0\left(1 + \left(\frac{f}{f_{crit,\ V}}\right)^4\right) \qquad (19)$$

and

$$q_C(f) = q_0\left(1 + \left(\frac{f}{f_{crit,\ q}}\right)^4\right) \qquad (20)$$

respectively. Here V_0 and q_0, are low-frequency limits of V_C and q_C, while $f_{crit,\ V}$ and $f_{crit,\ q}$ are frequencies, chosen so that $V_C(f_{crit,\ V})$ and $q_C(f_{crit,\ q})$ will be $2V_0$ and $2q_0$ respectively. The values of all fitting parameters with associated errors are given in Table II. Here, little change is observed in either q_0 or V_0 between devices #2 to #5, indicating little dependence on conductivity within the samples analyzed. It should also be noted that at low frequencies the wave number q_0 ($\approx$ 0.34μm^{-1}) is approximately $\frac{2\pi}{d}$, where d is the device spacing, indicating that the EHDI rolls are approximately circular.

The pure MLC 2081 sample (#1) does not appear to follow the 4th power dependency, described by equations (19) and (20), whilst also showing different textures. Comparing this to previously published work[35,51], it is believed that this is because the sample is within the dielectric regime of electroconvection (see figure 2) [38,42], where the type of analysis performed on the doped systems becomes unsuitable. The textures created in the pure sample's dielectric regime were distinctly less uniform and had visually lower contrast, indicating more limited use as efficient diffraction gratings, although a wide range of q_C values was observed.

Table I: Summary of the dielectric characterization of all devices, including; measured mass fraction of TBATPB (Φ), σ_0 found by fitting $\sigma(T)$ with equation 18, ε' (T=26 °C) values, and measured device spacing (d). Planar ~20 μm samples (#1-5) are ranked by value σ_0. The table also includes device #6 (pure MLC 2081 in ~20 μm homeotropic cell), #7(10 μm planar) and #8 (5μm planar). Due to in general thicker samples leading to more accurate dielectric measurements, the values of ε' and σ_0 in #8 were taken to be the same as #7 as they were taken from the same sample of LC.

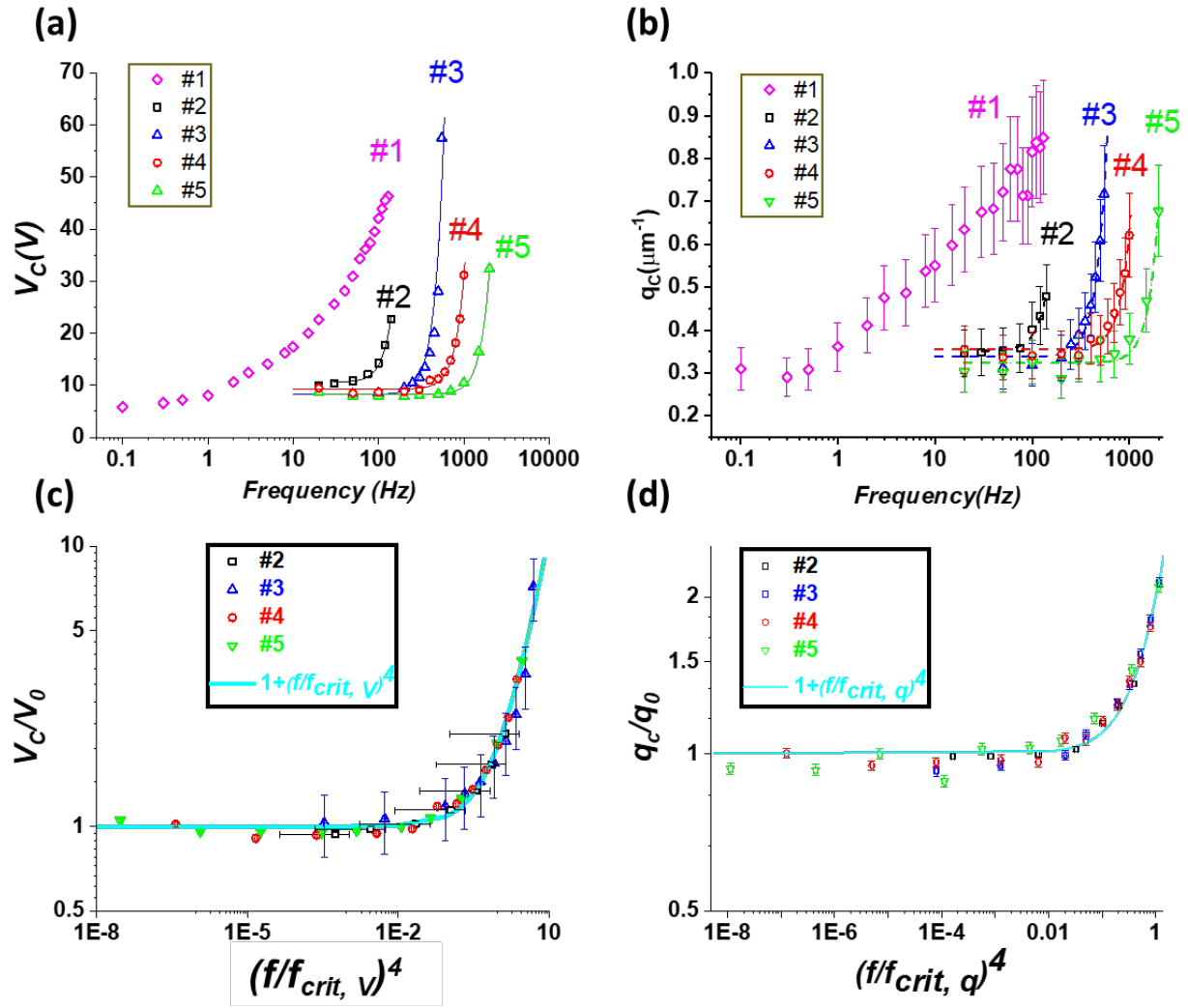| Device number	#1 (PL)	#2 (PL)	#3 (PL)	#4 (PL)	#5 (PL)	#6 (HT)	#7 (PL)	#8 (PL)
Φ(%)	0	0.5	0.3	2.3	1.0	0	0.6	0.6
σ_0(S/m)	(1.7 ± 0.5) x 10^{-2}	(7 ± 3) x10^{-2}	(1.5 ± 0.5)	(1.0 ± 0.2) x10^{2}	(6 ± 3)x10^{4}	(3 ± 1)x10^{-2}	(9 ± 1)	(9 ± 1)
ε' [52] (T=26°C)	6.0±0.3	6.4±0.3	6.6±0.3	6.6±0.3	6.4±0.3	3.1±0.2	6.8±0.5	6.8±0.5
$d(\mu m)$	19.6±0.2	19.2±0.2	18.9±0.3	18.9±0.1	19.1±0.2	18.1±0.2	10±0.2	4.9±0.2

FIG. 5 Plots of critical voltage and wave vectors in samples #1-5 at T=26°C. (a) Shows V_c values as functions of frequency. All but #1 are fit with equation 19, with which good agreement was found (b) Shows q_C as a function of frequency, similarly fitted with equation (20). (c) and (d) show reduced plots of #2 to #5 from values of V_0, q_0, $f_{crit, V}$ and $f_{crit, q}$ found from fittings (see table II) shown in (a) and (b). These are compared to $1+(f/f_{crit})^4$ line shown as cyan.

Figures 5c and 5d show V_C/V_0 and q_C/q_0 values plotted against $(f/f_{crit, V})^4$, and $(f/f_{crit, q})^4$ in devices #2 to #5, respectively. These show good agreement with the lines $1+ (f/f_{crit})^4$ vs. $(f/f_{crit})^4$, which is also plotted. This agreement indicates that equations (19) and (20) are suitable empirical descriptions of the experimental results.
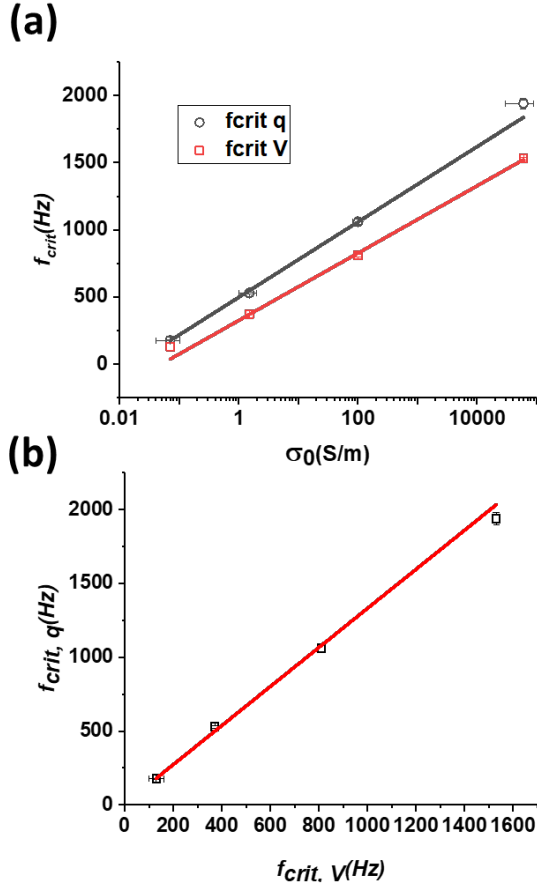

(a)

(b)

FIG. 6 Plots of the critical frequencies obtained from $V_C(f)$ and $q_C(f)$ by fitting data shown in figure 5 to equations (19) and (20) respectively. (a) $f_{crit, V}$ and $f_{crit, q}$ plotted against σ_0. (b) Plot of $f_{crit,q}$ against $f_{crit, V}$, where a linear dependence is observed.

The role of device conductivity is seen to strongly influence values $f_{crit, V}$ and $f_{crit, q}$, with higher values of σ_0 increasing values of both f_{crit}. These are plotted against σ_0 in figure 6a where fits:

$$f_{crit,V} = \alpha_V log_{10}\sigma_0 + c_V \qquad (21)$$

and

$$f_{crit,q} = \alpha_q log_{10}\sigma_0 + c_q \qquad (22)$$

are used. In these fits, the constants α_V, α_q, c_V and c_q from equations (21) and (22) are found to be: 250±5Hz, 280±10Hz, 326±5Hz and 500±10Hz, respectively. Figure 6b plots $f_{crit, V}$ versus $f_{crit, q}$, where a linear dependence is observed, indicating,

$$f_{crit,q} = \beta f_{crit,V} + c, \qquad (23)$$

where β and c are constants, found to be 1.33±0.05 Hz and 0±10Hz, respectively. The value of c indicates that within experimental error:

$$f_{crit,q} = \beta f_{crit,V}. \qquad (24)$$

As can be seen from equations (19) and (20), the rates of change of both V_C and q_C are determined by their respective f_{crit} values. Equation (24) shows an intrinsic link between the increased V_C and resultant q_C values that occurs as the frequency is increased.

The fourth power frequency dependence of both V_C and q_C can be understood as follows. As shown in figure 1, the two adjacent and opposite ion channels act as two charged electrodes. These electrodes form a capacitor, with a dielectric LC material between them, on which an in-plane electric field is applied. For the reorientation of the LC, this capacitor requires sufficient charging to create a large enough field to overcome the effects of the material's inertia. Clearly, for this to occur, a sufficiently low frequency is required for a critical amount of charge to accumulate before the polarity changes. Assuming that this in-plane capacitor charges linearly with time, this frequency must be lower than the inverse of some characteristic transit time ($\tau_{transit}$):

$$f < \frac{1}{\tau_{transit}} \qquad (25)$$

If this required amount of charge is treated as a classical point charge in an electric field, the $\tau_{transit}$ should satisfy equation;

$$d = a \cdot (\tau_{transit})^2 = \frac{F}{m^*}(\tau_{transit})^2 \qquad (26)$$

$$= \frac{VQ}{dm^*}(\tau_{transit})^2$$

where d is the device spacing, a is the particle acceleration, F is the force, V is the voltage, m^* is the effective mass of the ions and Q is the required charge. Combining equations (25) and (26) gives:

$$f < \sqrt{\frac{VQ}{d^2m^*}} \qquad \Rightarrow \qquad V_C = \frac{d^2m^*}{Q}f^2|_{q=const}. \qquad (27)$$

In addition to this requirement is the effect of roll size. Classically, the centripetal force required for a particle to move in a circular fashion is:

$$F_{cent} = m^*\omega^2R = 2\pi m^*f^2\lambda, \qquad (28)$$

where ω is the angular frequency, and R is the radius of motion. For electroconvective rolls, $\lambda=2R$ and $\omega=2\pi f$. Assuming the force is constant but λ shrinks, q will have quadratic dependency:

$$q \sim \frac{1}{\lambda} \sim f^2 |_{V=const}. \qquad (29)$$

Combining these arguments with the observation that within the regime observed V_C and q_C are proportional to each other,

it is possible to state that due to the simultaneous increase in both q_C and V_C, we expect that both obey the relationship:

$$V_C \sim q_C \sim f^4. \qquad (30)$$

Table II. Shows results from the characterization of devices #2 to #5 using optical microscopy and diffraction analysis. Samples are ranked by their σ_0 values, taken from fittings shown in figure 4. Microscopy results were taken at $T_{microscopy}$, where values; $f_{crit, V}$, V_0, $f_{crit, q}$, and q_0 were obtained by fitting to equations *(19)* and *(20)*. Diffraction analysis was undertaken at $T_{diffraction}$, results of which were fitted with equation (31) to obtain values of $f_{crit, \theta}$, and $sin\theta_{m=2,0}$.

Device number	#2	#3	#4	#5
σ_0(S/m)	$(7\pm3) \times 10^{-2}$	(1.5 ± 0.5)	$(1.0\pm0.2) \times 10^{2}$	$(6\pm3)\times10^{4}$
$T_{microscopy}$(°C)	26	26	26	26
$f_{crit, V}$ (Hz)	130±30	370±2	810±10	1530±9
V_0(V)	10.6±0.2	8±2	9.2±0.2	8.3±0.1
$f_{crit, q}$ (Hz)	177±3	529±8	1060±20	1940±40
q_0 (μm^{-1})	0.351±0.004	0.338±0.006	0.355±0.005	0.324±0.008
$T_{diffraction}$(°C)	~17	~17	~17	~17
$f_{crit, \theta}$ (Hz)	99±4	187±4	393±5	540±10
$Sin\theta_{0, m=2}$	0.071±0.02	0.081 ± 0.001	0.0733±0.0008	0.073±0.001

C. Diffraction analysis

When assessing device capability as a continuously variable diffraction grating, the second order diffraction spots ($m=\pm2$) were found to be the most efficient as has been shown previously[42–44]. This order was further studied to find the effect of driving frequency on the angle and efficiencies of the spots ($\theta_{m=\pm2}$ and $\xi_{=\pm2}$, respectively).

Figure 7a shows $sin\theta_{m=2}$ at V_C, plotted as a function of frequency in devices #2 to #5 (20 μm planar). Here continous steerage of the $m=2$ order is observed from ~4° to 8°, as frequency is varied in all devices. These data sets were fit with the equation:

$$sin\theta_{m=2} = sin\theta_{0, m=2}\left(1 + \left(\frac{f}{f_{crit,\theta}}\right)^4\right), \qquad (30)$$

where $sin\theta_{0, m=2}$ is the low-frequency limit of $sin\theta_{m=2}$ and $f_{crit, \theta}$ is the frequency were $sin\theta_{m=2}$ is double $sin\theta_{0, m=2}$. Equation (31) was chosen due to the combination of equations (9) and (20), and it appears to fit the data well. Figure 7b shows this data with scaled axes ($sin\theta_{m=2}/sin\theta_{0, m=2}$ against $(f/f_{crit, \theta})^4$). Similarly to V_C and q_C, a linear dependence following $1+(f/f_{crit, \theta})^4$ is demonstrated. Figure 7c shows the dependence of the fitted value $f_{crit, \theta}$ as a function of liquid crystal conductivity, σ_0. Here, a linear trend was observed with $log_{10}|\sigma_0|$ for all values. Figure 7d shows the device efficiency results, where in all samples, the efficiency dropped, typically from around 15% to 5%, as the frequency is increased, while angles varied from ~4° to 8°.
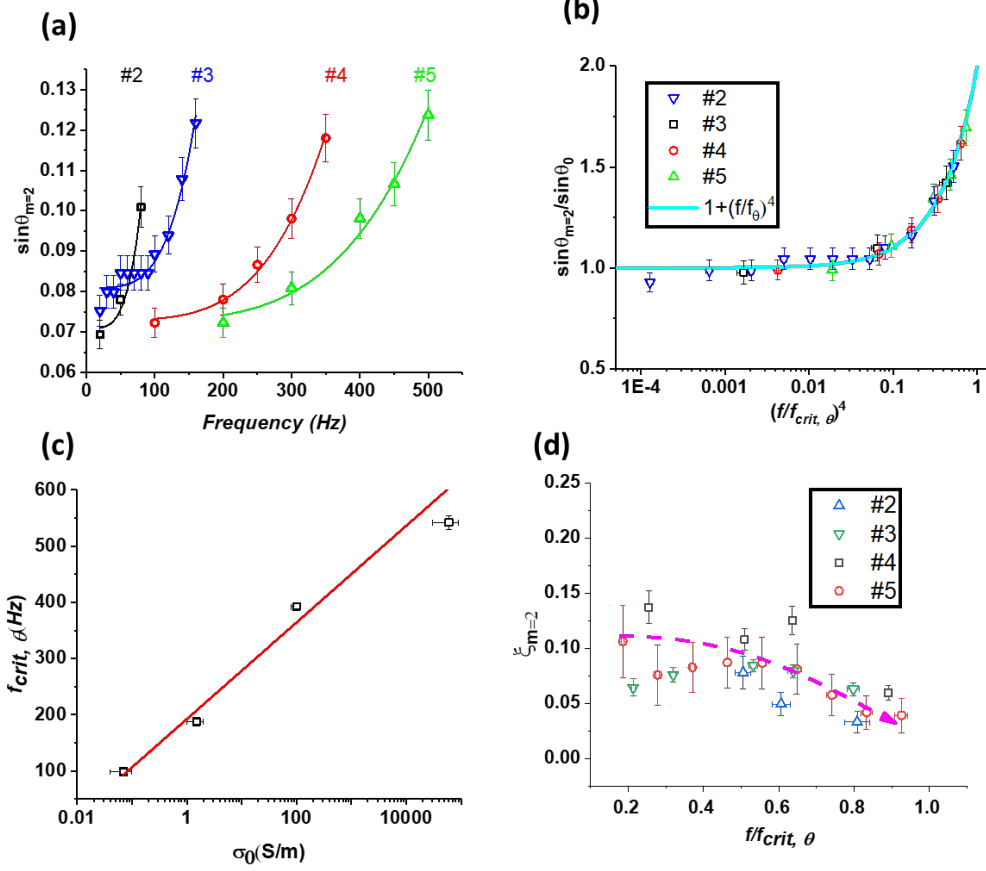
FIG. 7. Plots of steering angle and efficiency measurements of devices #2 to #5. (a) Diffraction angles as a function of frequency at V_C. These are fitted with equation (31) and acquired fitting parameters given in Table II. (b) Plot of reduced $sin\theta_{m=2}$ vs. frequency. (c) Plot of $f_{crit, \theta}$ vs. σ_0, where on a log scale linear dependence is observed. (d) Plot of efficiency of m=2 peaks as the frequency is varied. Here frequency is reduced by the factor $f_{crit, \theta}$ to show approximately similar behavior. A dashed line is included as a general guide to the eye.

D. Effects of device spacing

In order to examine the effect of device spacing, d, on diffractive performance, measurements of V_C, q_C, $\theta_{m=2}$ and $\xi_{m=2}$ were performed as functions of frequency on devices #3, #7 and #8 (planar devices of 20 μm, 10 μm and 5 μm spacing respectively). #3 was the 20 μm device chosen to compare, due to its similar σ_0 to the material placed in #7 and #8 (see table I).

For measurements of V_C and q_C, it was found that the 20 μm and 10 μm devices would undergo EC at 26°C while the 5μm would not. For this reason microscopy experiments on device #8 were performed at 76°C, as a lowering in material viscosity, reduces inertia to the EHDI state allowing it to occur at lower voltages. Results were fitted with equations (19) and (20), the results for which are given in Table III. Figure 8a shows the frequency dependence of q_C values, normalised by factor $f_{crit,q}$. Here as the frequency is increased q_C can be seen to vary from approximately $\frac{2\pi}{d}$, to around twice it's low-frequency value in all samples. Similarly, $sin\theta_{m=2}$ was fit to equation (31), and the results also given in Table III. Figure 8b shows $sin\theta_{m=2}$ as a function of reduced

frequency; here, as expected, it is observed that the thinner samples can attain wider angles (continuous ranges of such are shown in Table III). Due to the inability of the 5μm device to undergo EC at ambient temperatures, it was not possible to attain diffraction angles for device #8. However, as previously observed (see table II), q_0 has in all samples been dictated exclusively by the device spacing and the values q_C have appeared to have a limited range given by:

$$\frac{2\pi}{d} = q_0 < q_c < 2q_0 = \frac{4\pi}{d}, \tag{31}$$

indicating:

$$sin\theta_{0,m=2} < sin\theta_{m=2} < 2sin\theta_{0,m=2}. \tag{32}$$

10

Table III. Shows results from the characterization of devices #3, #7 and #8 using optical microscopy (taken at $T_{microscopy}$) and diffraction analysis (taken at $T_{diffraction}$). Samples are ranked by their σ_0 values, taken from fittings shown in figure 4. From microscopy, values; $f_{crit, V}$, V_0, $f_{crit, q}$, q_0, and λ_0 are given by fitting to equations *(19)* and *(20)*. From diffraction, values; $f_{crit, \theta}$, $sin\theta_{m=2,0}$ are given from fitting data to equation (31). In addition to this, the range of angles($\theta_{m=2}$) and matching efficiencies ($\xi_{m=2}$) are given[52].

Device number	#3	#7	#8
d(μm)	18.9±0.3	10±0.2	4.9±0.2
$T_{microscopy}$(°C)	26	26	76
$f_{crit, V}$ (Hz)	370±2	1140±20	5800±100
V_0(V)	8±2	9.6±0.4	10.6±0.1
$f_{crit, q}$ (Hz)	529±8	1660±10	6700±300
q_0(μm^{-1})	0.338±0.006	0.686±0.005	1.24±0.02
λ_0(μm)	18.6±0.3	9.2±0.1	5.0±0.1
$T_{diffraction}$(°C)	~17	~17	~17
$f_{crit, \theta}$ (Hz)	484±9	770±10	N/A
$Sin\theta_{m=2, 0}$	0.077±0.001	0.147±0.01	N/A
$\theta_{m=2}$ range	4°-8°	8°-14°	14°-30° (predicted)
$\xi_{m=2}$ range (corresponding to $\theta_{m=2}$ range)	15%-5%	5%-1%	<1% (predicted)

Eqn 32, allows a prediction of the behavior of $sin\theta_{m=2}$ in the thin sample #8 if it could be forced into an EHDI state at room temperature; this is included as the upper dashed line in figure 8b.

Table III shows the ranges of $\theta_{m=2}$ and $\xi_{m=2}$ demonstrated for the 10 and 20 μm devices (#7 and #3 respectively). Here it's shown that, although the 10 μm is capable of attaining wider angle steering (8° to 14°), it had correspondingly lower efficiency (5% to 1%), when compared to the 20 μm device (4° to 8° and 15% to 5%). This is taken to be due to lower contrast, and evidence that the rolls maintain circular shape as the frequency is increased, but the thickness of the modulating layer in the EHDI process is reducing. This means that a 20μm device being driven at a high frequency is approximately equivalent to a 10 μm driven at low frequency. This idea is illustrated in schematically in figure 8c.

(a)

$q_c (\mu m^{-1})$

2.5
2.0
1.5
1.0
0.5
0.0

△ 5μm (#8)
□ 10μm (#7)
○ 20μm(#3)

d

0.0 0.2 0.4 0.6 0.8 1.0 1.2

$f/f_{crit}, q$

(b)

$\sin\theta_{m=2}$

0.5
0.4
0.3
0.2
0.1

5μm (predicted)

$\xi_{m=2}$<1%

14°-30°

10μm

$\xi_{m=2}$=1%

8°-14°

20μm

$\xi_{m=2}$=5%

4°-8°

$\xi_{m=2}$=15%

-0.1 0.0 0.1 0.2 0.3 0.4 0.5 0.6 0.7 0.8

$(f/f_{crit}, \theta)^4$

(c)

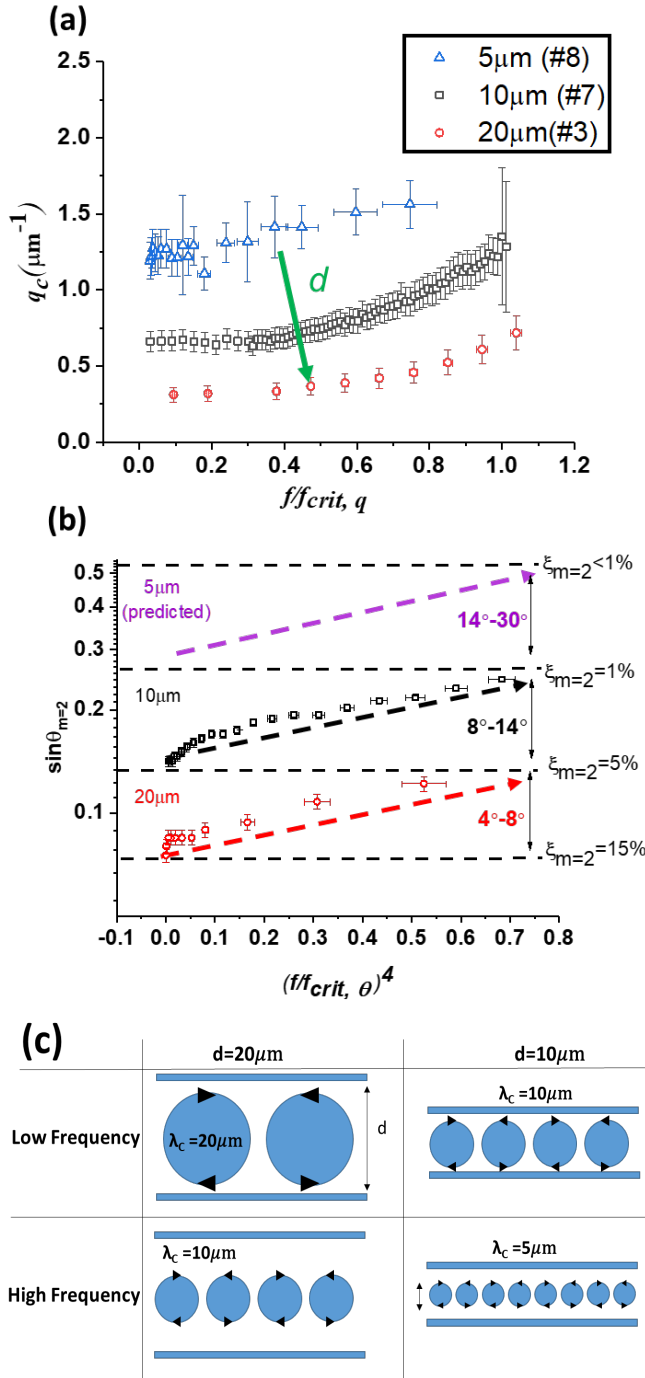|	d=20μm	d=10μm
Low Frequency	λ_c =20μm, d	λ_c =10μm
High Frequency	λ_c =10μm	λ_c =5μm

Fig. 8 Plot of thickness dependence of device operation in devices #3,7 and 8. (a) Plot of measured q_c values as a function of reduced frequency. These were fitted with equation 20 (fitting parameters are given in Table III). #3 and #7 were taken at 26 ^{O}C while #8 was at 76 ^{O}C as EHDI was not observed at ambient temperatures at standard operating voltages (<50 V). (b) Plot of diffraction steering angles of devices #3 and #7 against reduced frequency, ($f_{crit, \theta}$ obtained by fitting to equation 31, and is given in Table II). Results were taken in ambient laboratory conditions. The plot also shows the expected trajectory for the 5 μm device (#8) if the electroconvection had been able to occur at ambient temperatures. (c) A cartoon of the process causing the widening in steering angles, whilst lowering in efficiency as the frequency is increased. Due to

the rolls maintaining approximately circular shape, it's not possible to maintain large optical path difference, while having smaller rolls. It should be noted the similarity in optics of the high frequency 20 μm device and low frequency 10 μm device, this is supported by the very similar efficiencies and angles of m=2 diffraction peaks shown in (b).

E. Overview of device function and future optimization

1. Efficiency-wide angle trade-off

Overall, this work presents results that lead to the conclusion that nematic LC systems undergoing EHDI have disadvantages as functioning beam steering devices. Although continuous wide-angle steering (8° to 14°) has been demonstrated, and results indicate that it may be possible to increase the steering angle further, the corresponding drop in efficiency at high beam-steering angles is high and disadvantageous. These results are indicative that the rolls are maintaining circular motion, and the layer (thickness λ) undergoing EHDI, is becoming thinner as the frequency is increased: a shorter pitch of roll always results in a drop of contrast. Such a fundamental relationship is a significant drawback for a commercially viable device.

One simple solution to alleviate this issue is the use of a liquid crystal with higher birefringence to increase contrast and therefore efficiency, according to Eqn 11. Another solution could be the addition of functioning dopants such as dyes and nanorods[53–56]. Prior works show substantial contrast improvements, although with higher absolute efficiency losses, due to larger absorption of the incident light.

A third potential solution to this issue is through the judicious choice of the liquid crystal splay (K_{11}) and bend K_{33}) elastic constants. Although Eqn 2 uses the isotropic elastic constant approximation; we predict that an enhancement of splay elastic constant (K_{11})[57,58], would allow increased maximum contrast ($\Delta\phi$), due to increased reorientation persistence in the z-direction (see figure 9). In addition to this, it would be highly informative to examine materials with a very low bend elastic constant (K_{33}). This is due to the fact that such could force the EHDI state into adopting more elliptical shape, maintaining large contrast while increasing q_C (see figure 9), combining wider angle steering with higher efficiency.

In addition to elastic parameters, those of viscosity are also clearly important, particularly rotational viscosity as it is this that puts a torque onto the director setting ψ_{max}(equation 8). There is also the effect of anchoring strength of the alignment layer, which we believe should be minimized as much as possible whilst maintaining required alignment for the effect to occur.
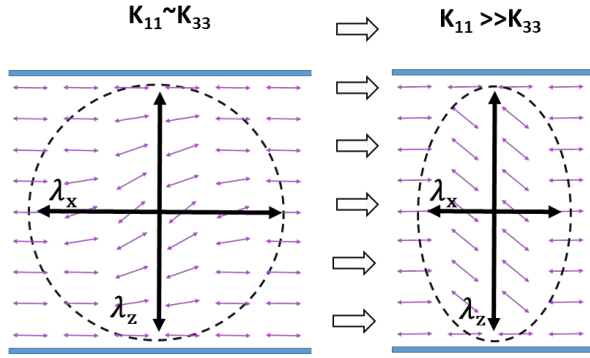
Figure 9. Shows schematic to illustrate how the choice of liquid crystal for specific elastic constants could optimize device performance, the director is represented by the purple double-headed arrows. Here two devices are shown, one such as the ones are examined in this work (left) and one with optimized elastic constants (right). We make the argument that the rolls need not be circular, but are in this work due to the K_{11} and K_{33} values not being specifically chosen to have any specific requirements, so being of similar values. We argue that it's likely that K_{11} dominates the amplitude of the phase grating (λ_x) while K_{33} dominates the pitch (λ_y). If therefore, a material was chosen to have very large K_{11} and small K_{33} device performance may be optimized. It is noted however, that here we have not considered what may be the more or similarly influential effects of the viscosities of the material and the anchoring strength of alignment layer.

2. Limitation in continuous steering

It is interesting that no device, regardless of conductivity or cell gap, attained a value of q that superseded $2q_0$. This is consistent with the theoretical findings of reference[34]. This sets the fundamental condition shown in equation (32), which limits the angle for continuous steerage. This can be alleviated by the use of thinner samples, albeit with reduced device efficiency.

3. Device longevity and reliability

In addition to the optical limitations, it is observed that over time, the doped samples of MLC 2081 experienced a lessening in the uniformity of alignment and increasing values of T_{NI} over time periods of several months. This would, of course, be undesirable for a functioning device. However, the increasing value of T_{NI} could be interpreted as being evidence that only one of the MLC 2081 components (corresponding to a lower T_{NI}) is breaking down over time, meaning again that judicious choice of materials can overcome this limitation.

The sensitivity of the EHDI state to temperature changes is also clearly undesirable, as for many beamsteering applications, it is required that the device function in a manner that is independent of temperature.

V. Conclusion

A liquid crystal system undergoing a dynamic pattern forming process has been examined for beem steering applications. The results have led to several new observations. Firstly, an apparent 4th power dependency in EHDI formation is found. Secondly, a systematic investigation of the limited range of roll wave vectors in the conduction state is provided and thirdly, simple yet compelling arguments that support the assertion that the roll structures maintain a circular shape even when driven to higher frequencies.

In addition to understanding the fundamental principles, this work demonstrates the benefits and limitations of systems undergoing electroconvection as potential spatial light modulators. A demonstration of the devices capable of acting as continually variable diffraction gratings with continuous steering angle is given. In agreement with previous works, the second order ($m=2$) was found to be the most efficient for all devices. From the viewpoint of creating functioning devices, an inverse relationship between steering angle and device efficiency is found. The devices have been shown to be capable of steering to at least 14° continuously, which is significantly better than many commercial devices. A discussion on the possibility of wider angles through tighter spaced devices is given. It is possible that such devices could be fabricated readily, through now, better-informed choice of LC material parameters tailored to the application. In addition, an overview of device optimization is provided including methodologies, which may greatly reduce or eliminate the current limitations. The effect of deliberate ionic doping of liquid crystals on the beam steering function of the devices is investigated and increased optical stability of patterns and correspondingly increased efficiency of the devices is found. This has allowed higher frequencies to be accessed than those reported in the literature previously.

13

REFERENCES

[1] E. Bodenschatz, W. Pesch, and G. Ahlers, Annu. Rev. Fluid Mech. **32**, 709 (2000).

[2] M. Parry, Phys. Rev. D - Part. Fields, Gravit. Cosmol. **62**, 8 (2000).

[3] Kapitza and P. L., in *Collect. Pap. P.L. Kapitza* (2013), pp. 714–725.

[4] K.E. Daniels, PhD Thesis 535 (2002).

[5] P.G. de. Gennes and J. Prost, *The Physics of Liquid Crystals*, 2nd ed. (Clarendon Press, 1993).

[6] R. Williams, Nature **199**, 273 (1963).

[7] G.H. Heilmeier, L.A. Zanoni, and L.A. Barton, Appl. Phys. Lett. **13**, 46 (1968).

[8] M. Schadt and W. Helfrich, Appl. Phys. Lett. **18**, 127 (1971).

[9] Susumu Sato, Japanese J. Appl. Phys. Susumu Sato Jpn. J. Appl. Phys **18**, (1979).

[10] M. Wahle, B. Snow, J. Sargent, and J.C. Jones, Adv. Opt. Mater. **7**, 1801261 (2019).

[11] M. Honma, T. Nose, S. Yanase, R. Yamaguchi, and S. Sato, Opt. Express **17**, 10998 (2009).

[12] O. Pishnyak, S. Sato, and O.D. Lavrentovich, Appl. Opt. **45**, 4576 (2006).

[13] U. Efron, *Spatial Light Modulator Technology : Materials, Devices, and Applications* (Marcel Dekker, 1995).

[14] D.J. McKnight, K.M. Johnson, and R.A. Serati, Appl. Opt. **33**, 2775 (1994).

[15] K.M. Johnson, D.J. McKnight, and I. Underwood, IEEE J. Quantum Electron. **29**, 699 (1993).

[16] G.D. Love, Appl. Opt. **36**, 1517 (1997).

[17] Y. Song, R.M. Panas, and J.B. Hopkins, Precis. Eng. **51**, 729 (2018).

[18] P.F. McManamon, P.J. Bos, M.J. Escuti, J. Heikenfeld, S. Serati, H. Xie, and E.A. Watson, Proc. IEEE **97**, 1078 (2009).

[19] J. Stockley and S. Serati, SPIE Proc. **5550**, 32 (2004).

[20] L.K. Cotter, T.J. Drabik, R.J. Dillon, and M.A. Handschy, Opt. Lett. **15**, 291 (1990).

[21] V. Fréedericksz and V. Zolina, Trans. Faraday Soc. **29**, 919 (1933).

[22] T. Nose, S. Masuda, and S. Sato, Jpn. J. Appl. Phys. **31**, 1643 (1992).

[23] H.C. Lin, M.S. Chen, and Y.H. Lin, Trans. Electr. Electron. Mater. **12**, 234 (2011).

[24] R.G. Lindquist, J.H. Kulick, G.P. Nordin, J.M. Jarem, S.T. Kowel, M. Friends, and T.M. Leslie, Opt. Lett. **19**, 670 (1994).

[25] Z. Zhang, Z. You, and D. Chu, Light Sci. Appl. **3**, (2014).

[26] Z. Zhang, Z. You, and D. Chu, Light Sci. Appl. **3**, (2014).

[27] M. Wang, L. Zong, L. Mao, A. Marquez, Y. Ye, H. Zhao, and F. Vaquero Caballero, Photonics **4**, 22 (2017).

[28] S. Sinzinger and J. Jahns, *Microoptics* (Wiley-VCH, 2003).

[29] G.R. Fowles, *Introduction to Modern Optics* (Dover Publications, 1989).

[30] X. Xiang, J. Kim, and M.J. Escuti, Sci. Rep. **8**, 7202 (2018).

[31] M. Honma and T. Nose, Japanese J. Appl. Phys. Michinori Honma Toshiaki Nose Jpn. J. Appl. Phys **43**, (2004).

[32] X. Wang, D. Wilson, R. Muller, P. Maker, and D. Psaltis, Appl. Opt. **39**, 6545 (2000).

[33] L.M. Blinov, Le J. Phys. Colloq. **40**, C3 (1979).

[34] S.J. Tavener, T. Mullin, G.I. Blake, and K.A. Cliffe, Phys. Rev. E - Stat. Physics, Plasmas, Fluids, Relat. Interdiscip. Top. **63**, (2001).

[35] L.M. Blinov and V.G. Chigrinov, Springer-Verlag New York (1994).

[36] E.F. Carr, Mol. Cryst. **7**, 253 (1969).

[37] W. Helfrich, J. Chem. Phys. **52**, 4318 (2004).

[38] L. Kramer and W. Pesch, in (Springer, New York, NY, 1996), pp. 221–255.

[39] A. Buka, N. Eber, and W. Pesch, Electron. Cryst. Commun. 1 (2005).

[40] L.M. Blinov and V.G. Chigrinov, in (1994), pp. 235–307.

[41] B. Zhang and H. Kitzerow, J. Phys. Chem. B **120**, 6865 (2016).

[42] T. John, U. Behn, and R. Stannarius, Eur. Phys. J. B **35**, 267 (2003).

[43] R.A. Kashnow and J.E. Bigelow, Appl. Opt. **12**, 2302 (1973).

[44] C. Bohley, J. Heuer, and R. Stannarius, J. Opt. Soc. Am. A **22**, 2818 (2005).

[45] J.A. Kosmopoulos and H.M. Zenginoglou, Appl. Opt. **26**, 1714 (1987).

[46] S. Valyukh, V. Chigrinov, H.S. Kwok, and H. Arwin, Opt. Express **20**, 15209 (2012).

[47] R. Allen, Bloom; Daniel Louis, (5 November 1975).

[48] H. Naito, Y. Yokoyama, S. Murakami, M. Imai, M. Okuda, and A. Sugimura, Mol. Cryst. Liq. Cryst. Sci. Technol. Sect. A. Mol. Cryst. Liq. Cryst. **262**, 249 (1995).

[49] Y.K. Cho and S. Granick, J. Chem. Phys. **119**, 547 (2003).

[50] P. Ben Ishai, M.S. Talary, A. Caduff, E. Levy, and Y. Feldman, Meas. Sci. Technol. **24**, 102001 (2013).

[51] A. Buka, Phys. Scr. **1989**, 114 (1989).

[52] Merck quote a value for $\varepsilon_\perp$ of 8.1at 20 ^{O}C and 1 KHz. These measured values of 6.5±0.5 were completed at 26 ^{O}C without guard-ring electrodes giving acceptable agreement.

[53] M. Shasti, J.T. Gleeson, and P. Luchette, Liq. Cryst. (2019).

[54] H. Hidehiro, T. Uchida, and Y. Shibata, Jpn. J. Appl. Phys. **24**, 299 (1985).

[55] E.I.L. Jull and H.F. Gleeson, Opt. Express (2018).

[56] K.J. Wu, K.C. Chu, C.Y. Chao, Y.F. Chen, C.W. Lai, C.C. Kang, C.Y. Chen, and P.T. Chou, Nano Lett. **7**, 1908 (2007).

[57] F.C. Frank, Discuss. Faraday Soc. **25**, 19 (1958).

[58] C.W. Oseen, Trans. Faraday Soc. **29**, 883 (1933).